

Analysis of RC walls with a mixed formulation frame finite element

Afsin Saritas^{*1} and Filip C. Filippou²

¹Department of Civil Engineering, Middle East Technical University, Ankara 06800, Turkey

²Department of Civil and Environmental Engineering, University of California, Berkeley, CA 94720, USA

(Received Jun 11, 2012, Revised February 14, 2013, Accepted May 24, 2013)

Abstract. This paper presents a mixed formulation frame element with the assumptions of the Timoshenko shear beam theory for displacement field and that accounts for interaction between shear and normal stress at material level. Nonlinear response of the element is obtained by integration of section response, which in turn is obtained by integration of material response. Satisfaction of transverse equilibrium equations at section includes the interaction between concrete and transverse reinforcing steel. A 3d plastic damage model is implemented to describe the hysteretic behavior of concrete. Comparisons with available experimental data on RC structural walls confirm the accuracy of proposed method.

Keywords: shear behavior; finite element method; mixed formulation; frame finite element; shear walls

1. Introduction

The shear response of reinforced concrete (RC) structural walls is mainly affected by the compressive zone in the wall; where triaxial compression stress conditions arise that enhance the shear resistance. The presence of axial compression not only increases the axial and lateral stiffness of the wall, but also increases the lateral load carrying capacity with increasing height to width (aspect) ratio. The modeling of these actions can be accomplished either with microscopic or macroscopic models. Microscopic models depend on the detailed description of the material response, which is integrated in 2d or 3d continuum finite elements to give the global load-deformation response of the member. With the rapid advances in finite element theory and computer hardware technology many such models have been proposed in the last 40 years. While such models may be suitable for the response prediction of a single member under complex loading conditions, their use is prohibitively expensive for the response analysis of large structural systems. Macroscopic models simplify the structural member by introducing approximations and assumptions that take advantage of its stress and deformation states under typical loading conditions.

Rericha (1991) proposed a frame element model by using a displacement-based beam finite element within the framework of the Timoshenko beam theory. The study included transverse strains by satisfying the transverse equilibrium equations for concrete and transverse

*Corresponding author, Professor, E-mail: asaritas@metu.edu.tr

reinforcement. The constitutive equations used for concrete were based on an approach similar to the rotating crack models.

Petrangeli, Pinto *et al.* (1999) proposed a force-based beam element within the framework of the Timoshenko beam theory. They considered the interaction between axial force, shear force and bending moment through fiber discretization of the section. At a material point, the normal stress and shear stress were coupled through the multi-axial micro-plane concrete material model by Bazant and Prat (1988). The transverse strains were included by satisfying the transverse equilibrium equations of concrete and transverse reinforcing steel. In a follow-up paper, Petrangeli (1999) presented correlation studies showing that the inclusion of shear deformations causes additional pinching of the hysteretic behavior of RC members yielding in flexure.

The authors of the present study previously presented a force-based frame finite element model for analysis of shear critical RC beams (Filippou and Saritas 2006). A similar work was undertaken by Navarro Gregori, Miguel Sosa *et al.* (2007) using a displacement-based frame finite element model for the analysis of RC beams. In both studies the modified compression field theory by Vecchio and Collins (1986) was used to couple the normal and shear stress at a material point of the section. While these studies produced good results in the estimation of the ultimate strength of shear critical RC beams, they were not able to trace the post peak response due to the inability of the constitutive model to capture permanent deformations and damage.

Martinelli (2008) used a displacement-based element that adopts Timoshenko beam theory for the description of shear-flexure interaction in RC members, as well. Later, Saritas and Filippou (2009b) used a force-based beam element with a 3d plastic-damage concrete material model and accurately simulated the shear critical beams tested by Vecchio and Shim (2004), and they were able to trace the post-peak range, as well. In a recent study, Valipour and Foster (2010) considered a force-based frame element including shear effects for the analysis of RC columns. The main focus in their study was the lack of objectivity due to softening of concrete, where this issue was handled at the material level by the use of crack band approach.

The use of frame elements is less common for modeling of RC shear walls than of beams and columns. As the wall height to depth ratio decreases, the kinematics of wall deformation may not be represented accurately with a line element whose axis coincides with the wall centerline. It is worth to mention that above efforts directed on RC beams and columns could also be applied to the analysis of RC walls, as well. For that purpose, the literature survey on the use of frame elements on RC members is still valid in terms of element formulation. Focusing specifically on the analysis of RC walls with frame finite elements, Kotronis and Mazars (2005) used a displacement-based beam element to describe the response of RC walls yielding in flexure. For the 2d model they use the assumptions of the Euler-Bernoulli beam theory to derive the displacement field for the element. For the 3d model they use a displacement-based Timoshenko beam element developed by Friedman and Kosmatka (1993). The uniaxial concrete material model by La Borderie (1991) describes the stiffness degradation of concrete in the longitudinal direction, while the shear response remains elastic and uncoupled. For the coupling between normal and shear stress, they used a biaxial concrete damage model by Mazars (1986), which is, however, limited to monotonic behavior. In order to incorporate the biaxial material model in the beam element they make the assumption that the transverse normal strains can be obtained by multiplying the longitudinal strains with the Poisson ratio of concrete.

In a recent effort, Ceresa, Petrini *et al.* (2009) presented a frame element based on Timoshenko beam theory and displacement-based finite element approach for the analysis of RC members. To avoid shear locking phenomena, linear shape functions were enriched by the introduction of a

bubble function. In the study modified compression field theory by Vecchio and Collins (1986) was used for the interaction between normal and shear stress at material points of concrete. The study presented accurate results for the cyclic analysis of RC walls.

While above frame type models consider distributed inelasticity along element length, an alternative is the use of frame type element models with rigid or linear elastic behavior along element length in conjunction with axial, shear and rotational springs placed at certain locations to capture nonlinear material behavior, i.e. the use of lumped plasticity models. Vulcano and Bertero (1987) used such an approach to idealize the wall with three vertical line elements, which act in parallel and are connected by infinitely rigid beams at the ends of the wall. The outer elements are trusses representing the axial stiffness of the boundary columns. The central element is a macro-element composed of a horizontal, spring that represents the shear stiffness of the entire wall, and of a vertical and rotational spring representing the axial and flexural stiffness of the central wall panel, respectively. Ghobarah and Youssef (1999) represented the wall with four steel springs, four concrete springs, and a shear spring. The effect of the axial force and bending moment on the response of the shear spring was included by means of a sectional analysis based on the equations of the modified compression field theory (Vecchio and Collins 1986). The study focused on describing the strength deterioration of squat walls. In a later study, Orakcal and Wallace (2004) proposed such a model for the study of the flexure response of rectangular and T-shaped slender walls, where the model consists of several truss elements that act in parallel and are connected at the wall ends by infinitely rigid beams, and a shear spring that describes the shear response of the wall, which is assumed to be uncoupled from the flexural response. In a recent study by Lee, Jeong *et al.* (2012), experimental results of cyclic reversed lateral force test on a two-story reinforced concrete shear wall sub-assembly are simulated analytically by using the frame type elements with lumped plasticity models in PERFORM-3D program.

An alternative to the frame type modeling strategies is the use of general purpose finite element programs with their available solid finite element and multi-axial concrete material models. As mentioned before, this alternative is mostly applicable for the analysis of fairly small systems (mostly components, members) and not suitable for the analysis of large structural systems due to modeling difficulties and robustness issues. Such a study was recently presented by Kazak (2011), where ANSYS finite element program was used and the available plasticity material models were calibrated, and the dynamic response of a squat shear wall that had been tested on a shaking table as part of an experimental program conducted in Japan was analyzed in detail.

The work in this paper strikes a balance between the computational efficiency of frame type models and the accuracy of solid finite element models by proposing a frame finite element that accounts for the interaction of shear force, bending moment and axial force using a multi-axial constitutive material model for concrete based on plasticity and damage mechanics theories.

2. Frame finite element formulation

The frame finite element is cast starting from the force equilibrium relations. First, the differential equations of equilibrium for a beam element in the undeformed configuration is written

$$N' + w_x(x) = 0; \quad M' + V = 0; \quad V' + w_y(x) = 0 \quad (1)$$

where N , M , and V are the axial, flexure and shear forces at a section, respectively. Prime symbol

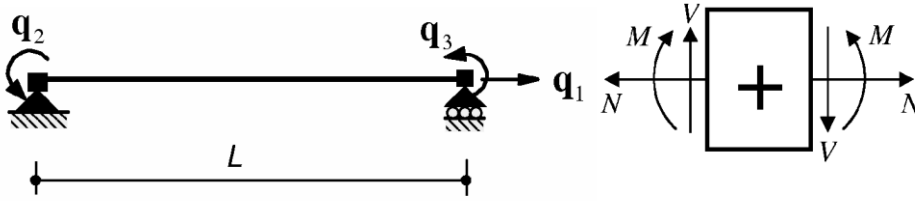


Fig. 1 Basic forces and deformations of beam element

in Eq. (1) denotes derivative with respect to x ; and w_x and w_y are the axial and transverse components of the distributed element load acting along the beam, respectively. The beam element axis corresponds to the x -axis in the formulation.

Under linear geometry, Eq. (1) can be solved independent of the displacements and of the material response. The boundary values in Fig. 1 are used as the basic element forces \mathbf{q} , and the equilibrium for the beam element with length L is expressed as follows

$$\underline{\mathbf{s}}(x) = \begin{pmatrix} N(x) \\ M(x) \\ V(x) \end{pmatrix} = \begin{bmatrix} 1 & 0 & 0 \\ 0 & x/L - 1 & x/L \\ 0 & -1/L & -1/L \end{bmatrix} \begin{pmatrix} q_1 \\ q_2 \\ q_3 \end{pmatrix} + \underline{\mathbf{s}}_p(x) = \underline{\mathbf{b}}(x)\mathbf{q} + \underline{\mathbf{s}}_p(x) \quad (2)$$

where $\underline{\mathbf{s}}(x)$ is the vector of the section forces, and $\underline{\mathbf{b}}(x)$ is the matrix of force interpolation functions. For uniform distributed element loading, the particular solution $\underline{\mathbf{s}}_p(x)$ can be easily found from equilibrium, and added to the right hand side of Eq. (2). The particular solution for uniform distributed element loading is presented by Saritas and Filippou (2009a).

The compatibility statement of the element is obtained from principle of virtual forces. From the equality between the external and internal work done as a result of the application of a virtual force system, i.e. $\delta \underline{\mathbf{s}}(x) = \underline{\mathbf{b}}(x)\delta \mathbf{q}$, the basic element deformations $\underline{\mathbf{v}}$ are obtained in terms of the section deformations $\underline{\mathbf{e}}(x)$ along the beam length L .

$$\underline{\mathbf{v}} = \int_L \underline{\mathbf{b}}^T(x) \underline{\mathbf{e}}(x) dx \quad (3)$$

where $\underline{\mathbf{e}}(x)$ is the vector of section deformations with following terms in given order: the axial deformation $\varepsilon_a(x)$, curvature $\kappa(x)$, and shear deformation $\gamma(x)$.

2.1 Element state determination

The element is implemented in a standard finite element program that is based on direct stiffness method of analysis. Any element implemented in such a platform should return its resisting forces and current stiffness matrix. The resisting forces in a displacement-based element are a function of the current deformations of the element, $\mathbf{q} = \mathbf{q}(\mathbf{v})$; therefore element state

determination is straightforward with displacement-based elements. However, in a force-based element such a direct relation cannot be obtained; because the current deformations can only be expressed as a function of the element resisting forces, $\underline{\mathbf{v}} = \underline{\mathbf{v}}(\underline{\mathbf{q}})$.

The element response is obtained from the fact that the given element deformations $\hat{\underline{\mathbf{v}}}$ should be equal to the element deformations compatible with element forces, i.e., $\hat{\underline{\mathbf{v}}} - \underline{\mathbf{v}}(\underline{\mathbf{q}}) = \mathbf{0}$. The solution to this equality is achieved by linearization, and the following updating scheme with an iteration counter j is obtained.

$$\Delta \underline{\mathbf{q}}^{(j+1)} = \left[\underline{\mathbf{f}}^{(j)} \right]^{-1} \left(\hat{\underline{\mathbf{v}}} - \underline{\mathbf{v}}^{(j)} \right) \quad \text{and} \quad \underline{\mathbf{q}}^{(j+1)} = \underline{\mathbf{q}}^{(j)} + \Delta \underline{\mathbf{q}}^{(j+1)} \quad (4)$$

where $\underline{\mathbf{v}}$ in Eq. (4) is obtained from Eq. (3) with numerical integration at discrete sections.

Constitutive relations at the section level are mostly derived from section deformations, $\hat{\mathbf{s}} = \hat{\mathbf{s}}(\mathbf{e})$, where the hat notation signifies that these section forces are deformation dependent. However, the section forces of the force-based element are given by the basic element forces in Eq. (2), and we denote this as $\underline{\mathbf{s}} = \underline{\mathbf{b}} \underline{\mathbf{q}} + \underline{\mathbf{s}}_p$. These two relations should be equal to each other in order to obtain a compatible section response for given element forces, i.e., $\underline{\mathbf{s}} - \hat{\mathbf{s}}(\mathbf{e}) = \mathbf{0}$. The solution to this equality is achieved by linearization again. Iterations at the section and element level can be done in a nested fashion as suggested by Spacone, Filippou *et al.* (1996). Therefore, the section iteration counter is selected to follow the element iteration counter, j .

$$\Delta \underline{\mathbf{e}}^{(j+1)} = \left[\underline{\mathbf{k}}_s^{(j)} \right]^{-1} \left(\underline{\mathbf{b}} \underline{\mathbf{q}}^{(j+1)} + \underline{\mathbf{s}}_p - \hat{\mathbf{s}}(\underline{\mathbf{e}}^{(j)}) \right) \quad \text{and} \quad \underline{\mathbf{e}}^{(j+1)} = \underline{\mathbf{e}}^{(j)} + \Delta \underline{\mathbf{e}}^{(j+1)} \quad (5)$$

where $\underline{\mathbf{k}}_s$ is the section stiffness matrix.

In depth discussion on above solution algorithms is presented by Saritas and Soydas (2012). In that work, the element state determination algorithms for the force formulation elements are derived from a three-field variational principle presented by Taylor *et al.* (2003).

2.2 Section modeling

Most common RC members such as beams, columns or walls have regular symmetric and rectangular cross-sections. Strains at a material point on the section can be written with the kinematic assumptions of the Timoshenko beam theory modified here to include variation on the shear strain as follows

$$\underline{\boldsymbol{\varepsilon}}_m = \underline{\mathbf{a}}_s \underline{\mathbf{e}}, \quad \text{where} \quad \underline{\mathbf{a}}_s = \underline{\mathbf{a}}_s(y) = \begin{bmatrix} 1 & -y & 0 \\ 0 & 0 & \psi(y) \end{bmatrix} \quad (6)$$

where $\underline{\mathbf{e}} = [\varepsilon_a \quad \kappa \quad \gamma(x)]^T$ is the section deformation vector and $\underline{\boldsymbol{\varepsilon}}_m = [\varepsilon_{xx} \quad \gamma_{xy}]^T$ is the strain at the material point written in vector form. The axis y corresponds to the perpendicular direction to the element x -axis on the plane. If constant shear strain profile is assumed on the section, then the shear strain profile $\psi(y)$ is equal to $\sqrt{\alpha}$, where α is the shear correction coefficient that

depends on the geometry of the section area, and $\alpha = 5/6$ for a rectangular section. The shear strain profile of a homogeneous rectangular section with $2d$ total depth may be estimated with the following parabolic relation as presented by Saritas and Filippou (2009a)

$$\psi(y) = 5/4 \left(1 - 4y^2/d^2\right) \quad (7)$$

The section forces are derived from the section deformations, and the corresponding section stiffness matrix can be obtained from the integration of material values over the section as follows

$$\hat{\mathbf{S}} = [\hat{N} \quad \hat{M} \quad \hat{V}]^T = \int_A \mathbf{a}_s^T \boldsymbol{\sigma}_m dA \text{ and } \mathbf{k}_s = \frac{\partial \hat{\mathbf{s}}}{\partial \mathbf{e}} = \int_A \mathbf{a}_s^T(y) \mathbf{k}_m \mathbf{a}_s(y) dA \quad (8)$$

where $\boldsymbol{\sigma}_m = [\sigma_{xx} \quad \sigma_{xy}]^T$, and \mathbf{k}_m is the material tangent stiffness $\mathbf{k}_m = d\boldsymbol{\sigma}_m/d\boldsymbol{\varepsilon}_m$. The hat over the section forces in (8) distinguishes these from the section force values that satisfy the element equilibrium relations according to $\mathbf{s} = \mathbf{b}\mathbf{q} + \mathbf{s}_p$. This distinction results from the use of a mixed formulation in the development of the beam finite element. The components of the section stiffness matrix in Eq. (8) are fully coupled through the use of a multi-axial material model.

Gauss-quadrature, midpoint or trapezoidal rule can be used for the numerical evaluation of the integrals in Eq. (8). Under the fiber discretization of the cross section, an integration point i is characterized by the distance of its centroid y_i from the reference axis and the corresponding weight A_i . The 2d tangent material stiffness at integration point i with axial and shear strain contributions is

$$\mathbf{k}_{m,i} = \begin{bmatrix} k_{aa} & k_{as} \\ k_{sa} & k_{ss} \end{bmatrix}_i \quad (9)$$

Plugging in Eq. (9) into Eq. (8) yields the section stiffness, which is written out in detail to illustrate the coupling of axial and shear strain effects

$$\mathbf{k}_s = \sum_{i=1}^{nL} \begin{bmatrix} k_{aa,i} & -y_i k_{aa,i} & \psi(y_i) k_{as,i} \\ -y_i k_{aa,i} & y_i^2 k_{aa,i} & -y_i \psi(y_i) k_{as,i} \\ \psi(y_i) k_{sa,i} & -y_i \psi(y_i) k_{sa,i} & \psi(y_i)^2 k_{ss,i} \end{bmatrix} A_i \quad (10)$$

where nL is the number of layers in the section. The section stress resultants are written from Eq. (8) as follows

$$\hat{\mathbf{s}} = \begin{pmatrix} \hat{N} \\ \hat{M} \\ \hat{V} \end{pmatrix} = \sum_{i=1}^{nL} \left\{ \begin{pmatrix} \sigma_{xx,i} \\ -y_i \sigma_{xx,i} \\ \psi(y_i) \sigma_{xy,i} \end{pmatrix} A_i \right\} \quad (11)$$

3. Material model

In this study the coupling of normal and shear stresses at a concrete material point is achieved by the use of a 3d plastic damage model. In order to use the 3d stress-strain relations in a beam finite element, the stress conditions in a beam element should be imposed as a constraint on the 3d constitutive model. A detailed description of the material model and its implementation in a beam finite element is presented by Saritas and Filippou (2009b). In the following, we summarize the integration of the 3d material model and the condensation of the necessary stress components for the sake of completeness of current presentation.

3.1 Continuum equations for plastic-damage model

A plasticity model with small strain theory can be written as $\boldsymbol{\varepsilon} = \boldsymbol{\varepsilon}^e + \boldsymbol{\varepsilon}^p$, $\boldsymbol{\sigma} = \mathbf{E}\boldsymbol{\varepsilon}^e$, $\dot{\boldsymbol{\varepsilon}}^p = \dot{\lambda}\mathbf{m}(\boldsymbol{\sigma}, \boldsymbol{\kappa})$ and $\dot{\boldsymbol{\kappa}} = \dot{\lambda}\mathbf{p}(\boldsymbol{\sigma}, \boldsymbol{\kappa})$. Here $\boldsymbol{\varepsilon}$, $\boldsymbol{\varepsilon}^e$ and $\boldsymbol{\varepsilon}^p$ are the total, elastic and plastic strain tensors respectively, $\boldsymbol{\sigma}$ is the stress tensor, \mathbf{E} is the elastic stiffness tensor, \mathbf{m} is the flow vector, \mathbf{p} are the plastic moduli, and $\boldsymbol{\kappa}$ is the set of internal variables. In a damage model, the effective stress tensor $\bar{\boldsymbol{\sigma}}$ is defined in terms of a damage parameter D , such that $\boldsymbol{\sigma} = (1 - D)\bar{\boldsymbol{\sigma}}$. The plastic multiplier $\dot{\lambda}$ is determined from the Kuhn-Tucker loading/unloading conditions by replacing $\boldsymbol{\sigma}$ with $\bar{\boldsymbol{\sigma}}$: $F(\bar{\boldsymbol{\sigma}}, \boldsymbol{\kappa}) \leq 0$, $\dot{\lambda} \geq 0$ and $F(\bar{\boldsymbol{\sigma}}, \boldsymbol{\kappa})\dot{\lambda} = 0$, where F is the yield function defining admissible stress states.

3.2 Constitutive equations

In the work by Lee and Fenves (1998), two damage variables, one for tensile damage D_t , and other for compressive damage D_c are defined independently. The model has two internal damage variables, $\boldsymbol{\kappa} = [\kappa_t, \kappa_c]^T$ for tension and compression. The evolution of internal variables is defined in the principal stress space as

$$\dot{\boldsymbol{\kappa}} = \dot{\lambda} \mathbf{p}(\bar{\boldsymbol{\sigma}}, \boldsymbol{\kappa}); \mathbf{p} = \mathbf{h}(\bar{\boldsymbol{\sigma}}, \boldsymbol{\kappa}) \cdot \nabla_{\bar{\boldsymbol{\sigma}}} \phi(\bar{\boldsymbol{\sigma}}, \boldsymbol{\kappa}); \mathbf{h}(\bar{\boldsymbol{\sigma}}, \boldsymbol{\kappa}) \begin{bmatrix} r(\bar{\boldsymbol{\sigma}})f_t(\kappa_t)/g_t & 0 & 0 \\ 0 & 0 & (1 - r(\bar{\boldsymbol{\sigma}})f_c(\kappa_c)/g_c) \end{bmatrix} \quad (12)$$

A non-associative flow rule is necessary to control the dilatancy in modeling concrete. A hyperbolic form of the Drucker-Prager function is used for the plastic potential function $\phi(\bar{\boldsymbol{\sigma}}, \boldsymbol{\kappa})$ in (12), while the yield function $F(\bar{\boldsymbol{\sigma}}, \boldsymbol{\kappa})$ is the Barcelona model which is a combined geometric shape from two different Drucker-Prager type functions. In (12) g_N is the specific fracture energy normalized by the characteristic length l_N where $N \in \{t, c\}$, leading to $g_N = G_N/l_N$. In order to maintain objectivity in the results, l_N should be objective. For the case of the beam element formulation, the characteristic length is selected equal to the integration weight of the corresponding section, and objective results are obtained for the beam element as presented by Saritas and Filippou (2009b). The model by Lee and Fenves (1998) was recently improved by Omid and Lotfi (2010) in order to consider the possibility of large crack opening/closing during cyclic loadings.

3.3 Integration of damage evolution equations

The time integration of the relations with a backward Euler method results in the following residual expressions $\mathbf{R}_{\bar{\sigma}} = \bar{\sigma}_{n+1} + \lambda \mathbf{E} \mathbf{m}(\bar{\sigma}_{n+1}, \boldsymbol{\kappa}_{n+1}) - \bar{\sigma}_{n+1}^{Trial} = \mathbf{0}$, $\mathbf{R}_{\boldsymbol{\kappa}} = \boldsymbol{\kappa}_{n+1} + \lambda \mathbf{E} \mathbf{m}(\bar{\sigma}_{n+1}, \boldsymbol{\kappa}_{n+1}) - \boldsymbol{\kappa}_n = \mathbf{0}$ and $\mathbf{R}_{\Delta \lambda} = F(\bar{\sigma}_{n+1}, \boldsymbol{\kappa}_{n+1}) = 0$. For the solution of these nonlinear equations, linearization is used with an iterative scheme that makes use of sub-stepping. It is important to emphasize that the damage correction step is independent of the plastic correction steps. It is observed that the rate of convergence of plastic-damage concrete model is close to quadratic; however when a large step is imposed convergence rate drops to linear. In order to resolve these difficulties, solution algorithms are used in conjunction with sub-stepping strategies, and convergence is typically achieved in 3 to 5 iterations when nonlinearity exists. Further discussion on the convergence of algorithms is available in Saritas (2006).

3.4 Condensation of the 3D stress-strain relations for a frame element

The section response of the proposed beam element has two nonzero stress values, namely the normal and shear stress at a material point of the cross section. On the other hand, the material model has six stress components. For the case with transverse reinforcement, transverse equilibrium gives $\sigma_y = -\rho_{vy} f_{vy}$ and $\sigma_z = -\rho_{vz} f_{vz}$, where the transverse reinforcing ratio in the y and z directions is ρ_{vy} and ρ_{vz} and the steel stress is f_{vy} and f_{vz} , respectively. Thus the equilibrium of normal stresses in the transverse direction can be obtained by satisfying the following residuals: $R_y = \sigma_y + \rho_y f_{vy} = 0$ and $R_z = \sigma_z + \rho_z f_{vz} = 0$, where σ_y and σ_z are the normal stresses in concrete for given directions y and z, respectively. Linearization of these residuals with respect to an initial strain in the y and z directions gives the update scheme for the unknown transverse strain fields. The material stiffness \mathbf{k}_m in Eq. (9) is calculated by condensing out the stress and strain tensor components that do not appear in the beam formulation. To this end the material tangent is first set up with six components of stress and strain in incremental form, and the transverse strain increments are subsequently used to derive the condensed material stiffness for the converged state of residuals.

3.5 Selection of material parameters

The tensile strength and modulus of elasticity of concrete is usually expressed in proportion to the square root of the compressive strength f'_c . In this study, $0.33\sqrt{f'_c}$ (MPa) is used for the cracking strength as suggested by ACI Committee 318 (1989), and the elastic modulus of concrete is taken equal to $3925\sqrt{f'_c}$ (MPa).

The tensile fracture energy of concrete is provided by CEB (1991), and the suggested values are used throughout the analysis in this paper. The compressive fracture energy of concrete is affected by the maximum aggregate size, the average distance between aggregates and the compressive strength of concrete. Furthermore, the presence of reinforcing steel also changes the fracture energy in compression, if reinforced concrete is modeled as a composite material. Currently, there is not enough information on the compressive fracture energy value for plain and

reinforced concrete material models. Nakamura and Higai (2001) propose that the compressive fracture energy increase nonlinearly with compressive strength according to $G_f^c = 8.8\sqrt{f'_c}$ (MPa), where G_f^c is expressed in N/mm. The same authors also recommend the following relation between tensile and compressive fracture energy $G_f^c = 250G_f^t$. However, the use of these two relations for a given concrete compressive strength does not give results that are consistent with the tensile fracture energy values in CEB (1991). Because of the paucity of information on this issue, the compressive fracture energy for plain concrete is assumed in line with similar values used by Feenstra and De Borst (1996) and Lee and Fenves (1998). In the analysis of RC beams, Oller, Onate *et al.* (1990) considered 25000 N/m compressive fracture energy value, and in the analysis of RC walls, Oller, Onate *et al.* (1990) arbitrarily chose 50000 N/m value for compressive fracture energy for a concrete with 35 MPa compressive strength. It is worth to mention that the load-displacement responses of ductile yielding RC walls analyzed in this paper are not sensitive to slight variations of suggested values of tensile fracture energy by CEB. However, due to lack of data, selection of compressive fracture energy has an influence on the response of RC members. Further discussion of this influence is available in Saritas (2006).

4. Comparison studies with RC structural walls

The following comparison studies on RC walls include two short walls tested by Lefas, Kotsovos *et al.* (1990) under monotonic loading conditions, and a slender wall tested by Thomsen and Wallace (2004) under cyclic loading conditions. All of these walls had rectangular cross-section where a typical cross section is subdivided into cover regions, boundary zones and web regions as shown in Fig. 2.

Lefas, Kotsovos *et al.* (1990) tested short RC walls, where the level of the axial force in these tests was between 0 to 20% of the axial load capacity of the wall. The walls were connected to an upper and a lower beam. The upper and lower beams in Fig. 3 were both 1150 mm in length and 200 mm in width, and the upper beam had 150 mm depth, while the lower beam had 300 mm depth. The lower beam was properly reinforced in order to provide full restraint to the base of the wall. The upper beam serves for the application of axial and horizontal loads. Two walls with rectangular cross-section are selected for correlation studies, and these have the following geometric dimensions: 650 mm wide x 1300 mm high x 65 mm thick.

A typical cross section is subdivided into cover regions, boundary zones and web regions as shown in Fig. 2. 8 mm and 6.25 mm diameter steel bars were used in the vertical and horizontal directions, respectively. The boundary zones shown in Fig. 2 are confined with 4 mm diameter hoops. The horizontal and hoop bars were placed with a spacing of 115 mm over the wall height. These reinforcement values result in the following reinforcement ratios: ratio of horizontal reinforcement to gross concrete area of vertical section of wall web $\rho_{hor} = 0.8\%$; ratio of vertical web reinforcement to gross concrete area of horizontal section of wall web $\rho_{ver} = 2.5\%$; ratio of main flexural reinforcement to gross concrete area of edge element $\rho_{flex} = 3.3\%$; ratio of effective volume of confinement reinforcement to the volume of the core $\rho_s = 0.9\%$. The material properties of 8 mm reinforcement bars are provided in Table 1. The elastic modulus of steel is taken as 200 GPa throughout the analysis, and the ratio between ultimate and yield strength

resulted in a strain hardening ratio of 0.5% of the elastic modulus of steel.

With regards to the concrete material properties, only the compressive strength from cubic specimens was provided by Lefas, Kotsovos *et al.* (1990). The compressive strength of concrete for Walls SW21 and SW22 were provided in the experiment as 36.4 and 43 MPa, respectively. The cylinder strength of concrete is used in the analysis, and it is taken equal as 85% of the cube strength. The tensile strength and Young modulus are calculated from the reported compressive strength by $0.33\sqrt{f'_c}$ (MPa) and $3925\sqrt{f'_c}$ (MPa), respectively.

Both of the walls are analyzed with one element and 5 Gauss integration points (IP) along the wall height. 15 layers are used over the wall section to get the section stress resultants and stiffness. The location of these layers is obtained from midpoint integration rule. The distribution of the layers among the regions over the wall section as described in Fig. 2 is as follows: the web

Table 1 Material properties of reinforcement bars for RC Walls by Lefas *et al.* (1990)

Type	Yield strength (MPa)	Ultimate strength (MPa)
8 mm bar	470	565
6.25 mm bar	520	610
4 mm bar	420	490

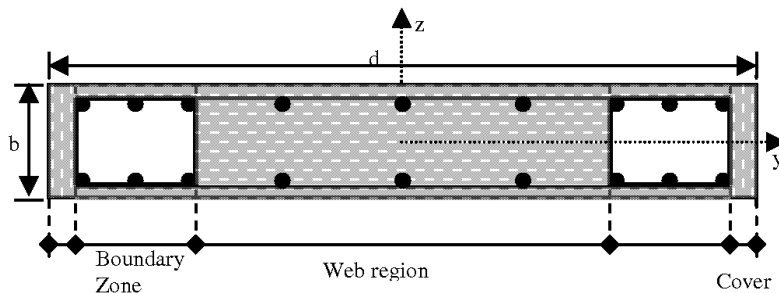


Fig. 2 Description of regions in RC wall cross-section

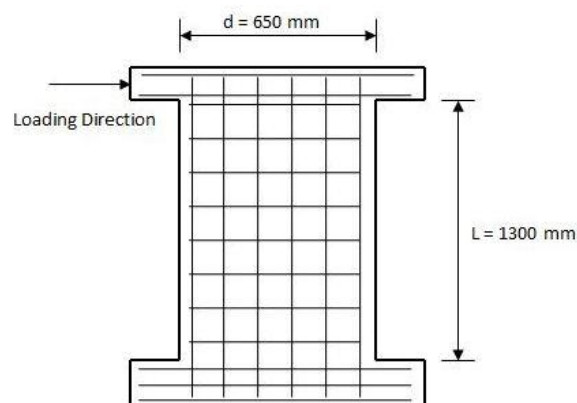


Fig. 3 Set up of Lefas *et al.* (1990) specimens

region is divided into 7 layers, each boundary zone has 3 layers, and each cover zone has 1 layer.

Wall specimen SW21 is loaded with zero axial load ($\nu=0$), and SW22 is loaded with 10% of the axial load capacity $A_g f_c'$ ($\nu=0.1$), where A_g is the gross area of the wall section.

The tensile fracture energy for SW21 is calculated from CEB (1991) as 80 N/m, and for SW22 as 90 N/m. The compressive fracture energy for both walls is assumed as 75000 N/m due to the high density of reinforcement in horizontal and vertical directions.

As can be seen from Fig. 4, not only the initial stiffness of the wall is represented accurately for both walls, but also the entire load-deformation curves of the experimental results are traced very closely by the analytical results.

The damage distribution of the wall specimen SW21 shows significant tensile damage in Fig. 5 where this can be related with the orientation of the plastic strains presented in Fig. 6. There was no significant spread of compression damage in the wall, and thus this is not presented. The rotation of the plastic strains over the wall height suggests the formation of compressive load path over the wall height. The analyzed walls go through significant flexure yielding and are ductile. In contrast to the orientation of strains in beams failing in flexure as presented in Saritas and Filippou (2009b), the orientation of strains in the walls is diagonal and shear cracks are distributed over the entire height of the wall.

The spread of compression damage in the walls is lower than the beams since the 3d state of compressive stresses delays the damage. The proposed model was able to capture these effects in the wall as a result of the use of a 3d concrete material model. Comparison of Fig. 7 with Fig. 5 reveals that the compressive force on wall SW22 reduced the spread of tensile damage over the wall height compared to wall SW21. The point numbers in Figs. 4 to 7 represent the loading step number during the nonlinear analysis of that member.

Furthermore, the stiffness increase as a result of the application of compressive load for the two cases of $\nu=0$ and $\nu=0.1$ multiple of axial load capacity $A_g f_c'$ on the wall is also evident in the load-deformation curves, and this increase is closely captured by the proposed model when results are compared with experimental data in Fig. 8.

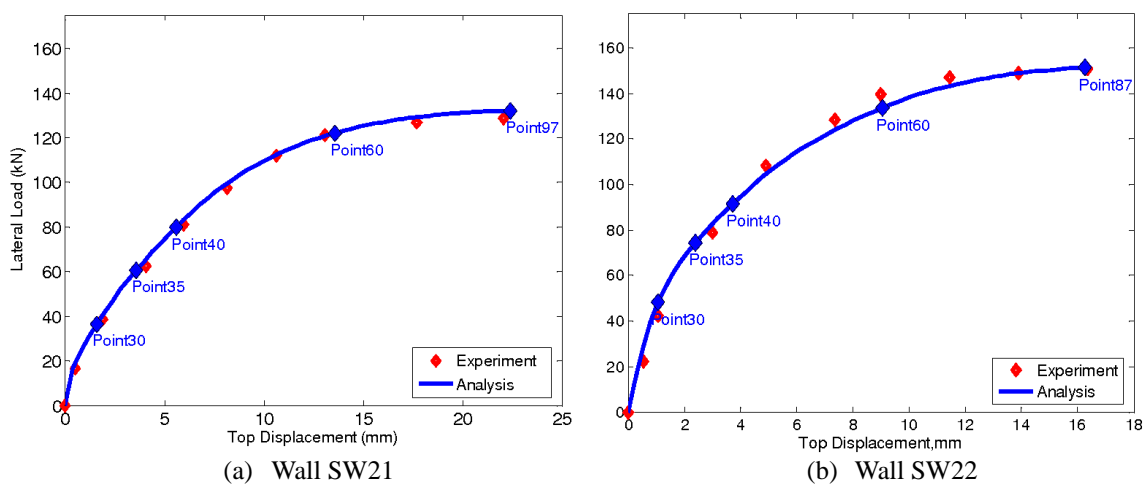


Fig. 4 Lateral load vs. top displacement response for walls SW21 & SW22 by Lefas *et al.* (1990)

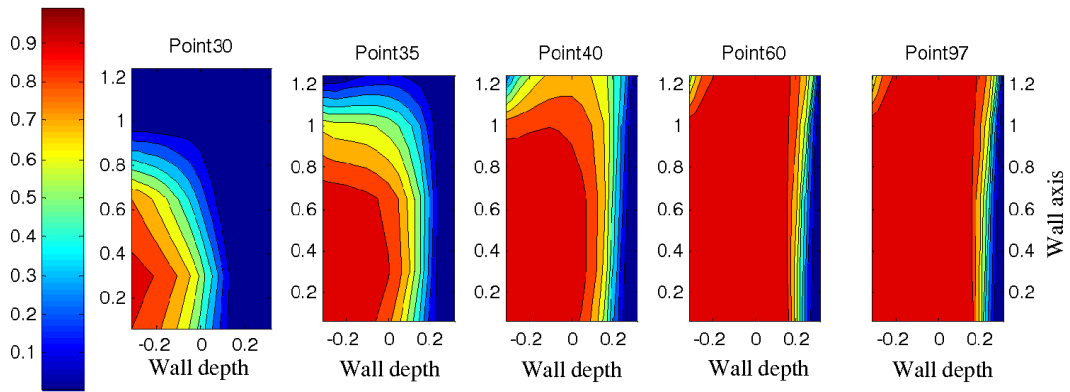


Fig. 5 Evolution of tensile damage distribution in numerical analysis for wall SW21 by Lefas *et al.* (1990)

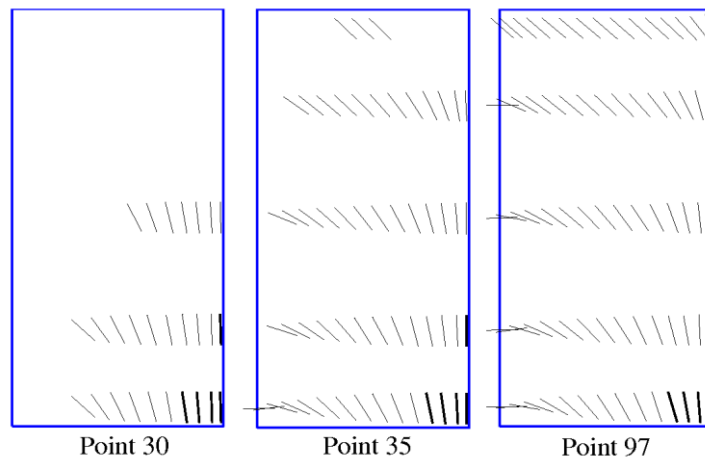


Fig. 6 Evolution of plastic strain directions in numerical analysis for wall SW21 by Lefas *et al.* (1990)

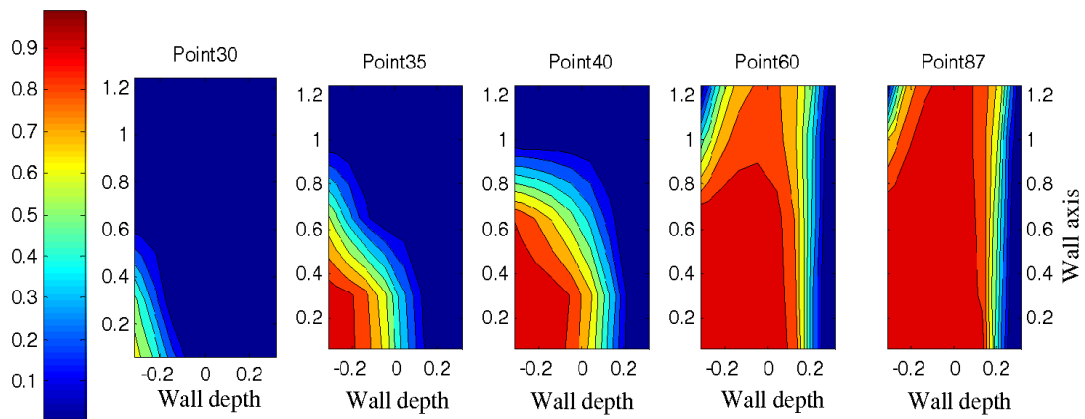


Fig. 7 Evolution of tensile damage distribution in numerical analysis for wall SW22 by Lefas *et al.* (1990)

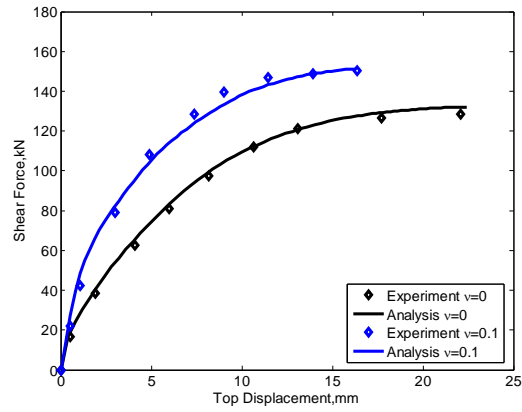


Fig. 8 Comparison of load-deformation responses of walls SW21 and SW22

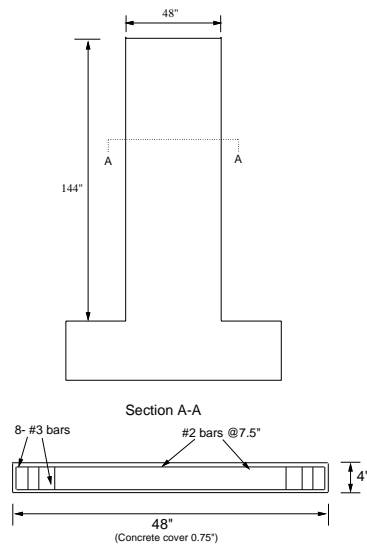


Fig. 9 Thomsen and Wallace (2004) specimen

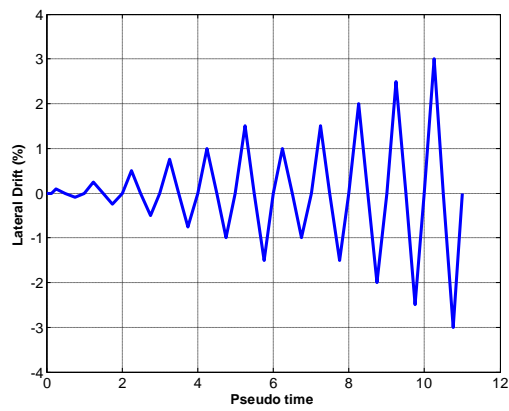


Fig. 10 Loading history of wall RW2 from Thomsen and Wallace (2004)

The comparison studies continue with the experimental work conducted by Thomsen and Wallace (2004). In that study, Thomsen and Wallace (2004) originally tested six slender RC wall specimens built to 1/4 scale, where only the four of the specimens without openings were presented in their study. The aspect ratio of these walls was 3 for all of the specimens. The walls included two walls with rectangular cross-section and two walls with T-shaped cross-section. The geometry and the configuration of the wall specimens RW1 and RW2 from Thomsen and Wallace (2004) are similar, and are shown in Fig. 9, where the cross-section detail is presented for specimen RW2. Both of these specimens showed significant flexural yielding for drift ratios in excess of 2% of the wall height. Buckling of the boundary longitudinal reinforcement was delayed in RW2 by the use of closer transverse hoops as compared to RW1. As the results were very similar for both walls, specimen RW2 is chosen for comparison with the analytical model.

A constant axial load of $0.07A_g f'_c$ was applied at the top of the wall, then the top of the wall is laterally cycled with the loading history shown in Fig. 10.

The yield strength of #2, #3 and the hoop bars were 414 MPa, and Young Modulus for steel is taken as 200 GPa in the analysis. The ultimate strength of #2 and #3 bars were 600 MPa. The longitudinal bars are modeled with the GMP model, where the strain hardening ratio for these two bars is calculated as 1%. The hoop bars are modeled with a bilinear hysteretic model, and the strain hardening ratio for these bars is taken as 0.5% due to its lower ultimate strength. The design compressive strength of concrete was 27.6 MPa; however compressive strength at the day of testing was reported as 42.8 MPa. The applied axial load on the wall was calculated from the design strength. The tensile strength and Young modulus are calculated from the test day compressive strength as $0.33\sqrt{f'_c}$ (MPa) and $3925\sqrt{f'_c}$ (MPa), respectively. The maximum aggregate size for concrete was reported as 10 mm in the test, thus the tensile fracture energy is calculated from CEB (1991) as 75 N/m. The compressive fracture energy of concrete is assumed as 50000 N/m, 40000 N/m in the boundary zone, web region, respectively. The compressive fracture energy for the cover regions is assumed as 10000 N/m.

The wall is analyzed with one element and 5 Gauss integration points (IP) along the beam. The wall section is subdivided into 15 layers where the locations are calculated from midpoint integration rule, and the subdivision is based on the relative length of each region with respect to the wall depth. The cover regions at the top and bottom are each represented with a single layer, each boundary zone is subdivided into 2 layers, and the web region is represented with 9 layers.

The lateral load versus the top displacement relations from the analysis and the test are presented in Fig. 11. The ultimate lateral load is perfectly captured with the proposed model, and the model is able to predict stiffness degradation in the wall. The unloading branches in the analytical response deviate from the measured response as seen in the figures due to the linear unloading curves in the plastic-damage concrete model used in this paper. Furthermore, the longitudinal steel bars have significant influence in the unloading and pinching responses, as well. In order to capture this response more closely in the load-displacement curves, unloading and then reloading behavior resulting from the constitutive models should reflect prior occurrence of nonlinearities better. Because the proposed model does not initiate unloading behavior earlier, the pinching effect is more pronounced in the analytical results. Despite this slight discrepancy, the analytical model has captured the overall nonlinear behavior and the absorbed energy very well with a consistent selection of material parameters.

The evolution of tensile damage in the wall at various instances in the load-deformation response in Fig. 12 is presented in Fig. 13, where the point numbers represent the loading

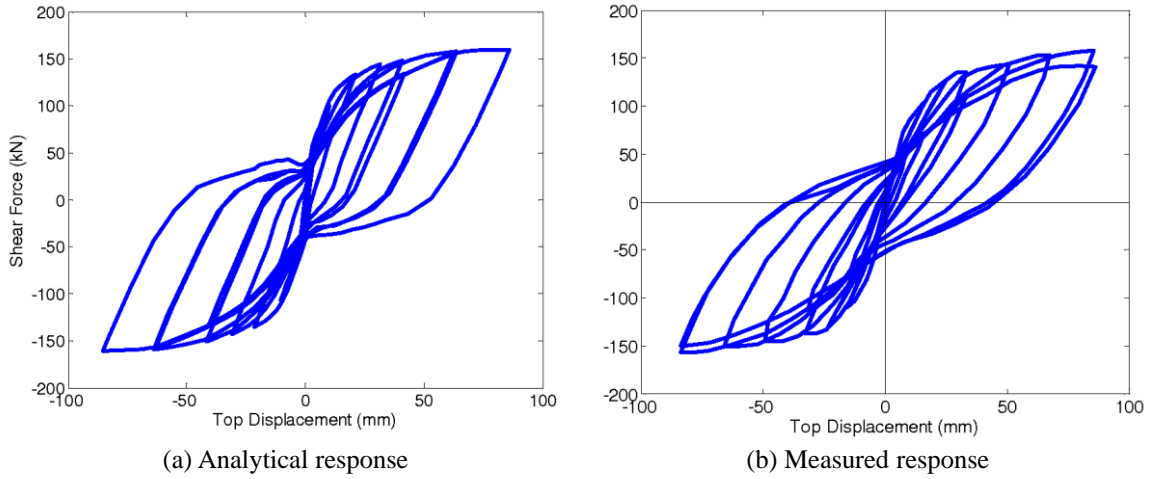


Fig. 11 Shear force-top displacement responses for wall RW2 of thomsen and wallace (2004)

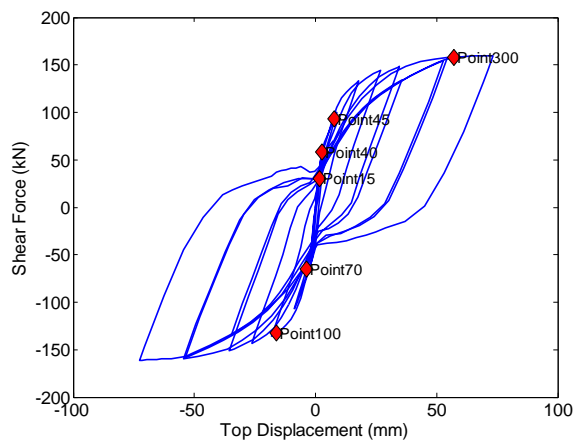


Fig. 12 Location of the points for the damage distribution graphs

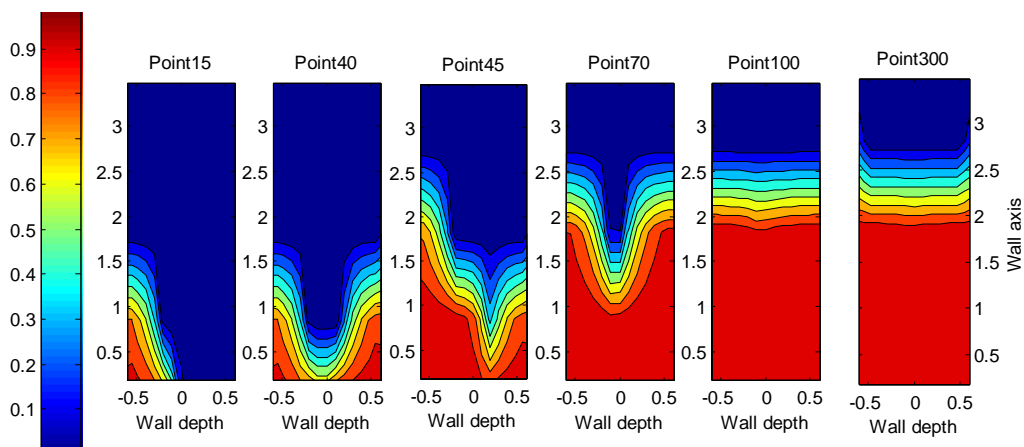


Fig. 13 Evolution of tensile damage

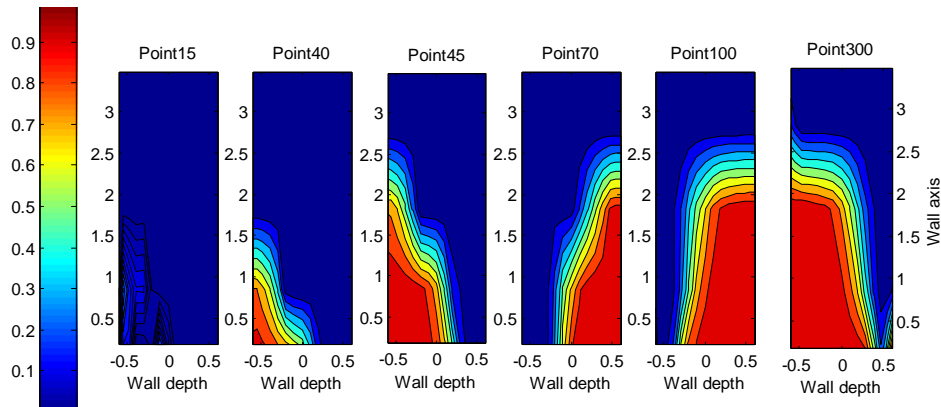


Fig. 14 Evolution of total damage

step number during the nonlinear analysis of that member. The compression damage distribution is not presented in here, and is only apparent at the outer faces of the wall at later phases of the deformations (its influence is visible in the total compression damage distribution in Fig. 14 for the response of analysis point 300). The evolution of tensile damage is much more pronounced, and the spread of tensile damage occurs quickly in the initial phases of the loading. At analysis point 100 which corresponds to 0.5% of lateral drift, the spread of tensile damage stabilizes over the wall height. The distribution of total damage in Fig. 14 clearly shows the cyclic nature of the total damage parameter, where the total damage D is calculated from tensile damage D_t and compressive damage D_c through the use of equation $D = 1 - (1 - D_t)(1 - D_c)$. More in depth discussion on the plastic damage concrete model used is available in Saritas (2006).

It is worth to emphasize that the analysis conducted in this paper did not consider RC walls where softening behavior is observed. Such an effort in capturing the post-peak softening response of RC members through the use of proposed models was presented in an earlier study by the authors in the analysis of shear critical RC beams (Saritas and Filippou 2009b).

6. Conclusions

The proposed model is able to capture the overall load-deformation response of RC structural walls of varying aspect ratios. The analyzed walls are ductile and go through significant flexural yielding. The overall response in the elastic and inelastic range is captured well with a single element discretization of the member without shear locking, while equally satisfactory agreement is obtained for local response measures such as tensile and compression damage distributions, and orientation of principal strains and cracks as well as concrete and reinforcing steel stresses.

References

- ACI Committee 318 (1989), Building Code Requirements for Reinforced Concrete (ACI 318-89), Detroit, American Concrete Institute.
- Bazant, Z.P. and Prat, P.C. (1988), "Microplane model for brittle-plastic material .1. Theory", *J. Eng. Mech.*

- ASCE, **114**(10), 1672-1687.
- CEB (1991), CEB-FIP model code 1990 - final draft. Lausanne, CEB.
- Ceresa, P., Petrini, L., Pinho, R. and Sousa, R. (2009), "A fibre flexure-shear model for seismic analysis of RC-framed structures", *Earthq. Struct. Dyn.*, **38**(5), 565-586.
- Feenstra, P.H. and De Borst, R. (1996), "A Composite plasticity model for concrete", *Int. J. Solids Struct.*, **33**(5), 707-730.
- Filippou, F.C. and Saritas, A. (2006), "A beam finite element for shear-critical RC beams", *ACI Spec. Publication.*, **37**, 295-310.
- Friedman, Z. and Kosmatka, J.B. (1993), "An improved 2-Node timoshenko beam finite-element", *Comput. Struct.*, **47**(3), 473-481.
- Ghobarah, A. and Youssef, M. (1999), "Modelling of reinforced concrete structural walls", *Eng. Struct.*, **21**(10), 912-923.
- Kazak, I. (2011), "Finite element analysis of shear-critical reinforced concrete walls", *Comput. Concr.*, **8**(2).
- Kotronis, P. and Mazars, J. (2005), "Simplified modelling strategies to simulate the dynamic behaviour of R/C walls", *J. Earthq. Eng.*, **9**(2), 285-306.
- La Borderie, C.L. (1991), Phénomènes unilatéraux dans un matériau endommageable: modélisation et application à l'analyse des structures en béton, Université Paris.
- Lee, H.S., Jeong, D.H. and Hwang, K.R. (2012), "Analytical simulation of reversed cyclic lateral behaviors of an RC shear wall sub-assembly", *Comput. Concr.*, **10**(2).
- Lee, J. and Fenves, G.L. (1998), "Plastic-damage Model for Cyclic Loading of Concrete Structures", *J. Eng. Mech. -ASCE*, **124**(8), 892-900.
- Lefas, I.D., Kotsovos, M.D. and Ambraseys, N.N. (1990), "Behavior of reinforced-concrete structural walls - strength, Deformation Characteristics, and Failure Mechanism", *ACI Struct. J.*, **87**(1), 23-31.
- Martinelli, L. (2008), "Modeling of shear-flexure interaction in reinforced concrete elements subjected to cyclic lateral loading", *ACI Struct. J.*, **105**(6), 675-684.
- Mazars, J. (1986), "A description of microscale and macroscale damage of concrete structures", *Eng. Fract. Mech.*, **25**(5-6), 729-737.
- Nakamura, H. and Higai, T. (2001), Compressive Fracture Energy and Fracture Zone Length of Concrete. Modeling of Inelastic Behavior of RC Structures under Seismic Loads. P.B. Shing and T. Tanabe, ASCE: 471-487.
- Navarro Gregori, J., Miguel Sosa, P., Fernandez Prada, M.A. and Filippou, F.C. (2007), "A 3d numerical model for reinforced and prestressed concrete elements subjected to axial, bending, shear and torsional loading", *Eng. Struct.*, **29**(12), 3404-3419.
- Oller, S., Onate, E., Oliver, J. and Lubliner, J. (1990), "Finite element nonlinear analysis of concrete structures using a "plastic damage model", *Eng. Fract. Mech.*, **35**(1/2/3), 219-231.
- Omidi, O. and Lotfi, V. (2010), "Numerical Analysis of Cyclically Loaded Concrete Under Large Tensile Strains by the Plastic-Damage Model" SCIENTIA IRANICA TRANSACTION A-CIVIL ENGINEERING, **17**(3), 194-208.
- Orakcal, K. and Wallace, J.W. (2004), Modeling of Slender Reinforced Concrete Walls, Proceeding of the 13th World Conference on Earthquake Engineering, Vancouver.
- Petrangeli, M. (1999), "Fiber element for cyclic bending and shear of RC structures. II: Verification", *J. Struct. Eng. ASCE*, **125**(9), 1002-1009.
- Petrangeli, M., Pinto, P.E. and Ciampi, V. (1999), "Fiber element for cyclic bending and shear of RC structures. I: Theory", *J. Struct. Eng. ASCE*, **125**(9), 994-1001.
- Rericha, P. (1991), "Layer Model of Bending-Shear Failure in Rc Plates and Beams", *J. Struct. Eng. ASCE*, **117**(10), 2865-2883.
- Saritas, A. (2006), Mixed Formulation Frame Element for Shear Critical Steel and Reinforced Concrete Members, Ph.D. Dissertation, University of California, Berkeley.
- Saritas, A. and Filippou, F.C. (2009a), "Inelastic axial-flexure-shear coupling in a mixed formulation beam finite element", *Int. J. Non-Linear Mech.*, **44**(8), 913-922.
- Saritas, A. and Filippou, F.C. (2009b), "Numerical integration of a class of 3d plastic-damage concrete

- models and condensation of 3d stress-strain relations for use in beam finite elements”, *Eng. Struct.*, **31**(10), 2327-2336.
- Saritas, A. and Soydas, O. (2012), “Variational base and solution strategies for nonlinear force-based beam finite elements”, *Int. J. Non-Linear Mech.*, **47**, 54-64
- Spacone, E., Filippou, F.C. and Taucer, F.F. (1996), “Fiber beam-column model for nonlinear analysis of RC frames: I: Formulation”, *Earthq. Eng. Struct. Dyn.*, **25**(7), 711-725.
- Taylor, R.L., Filippou, F.C., Saritas, A. and Auricchio, F. (2003), “Mixed finite element method for beam and frame problems”, *Comput. Mech.*, **31**(1-2), 192-203.
- Thomsen, J.H. and Wallace, J.W. (2004), “Displacement-based design of slender reinforced concrete structural walls-experimental verification”, *J. Struct. Eng.-ASCE*, **130**(4), 618-630.
- Valipour, H.R. and Foster, M.P. (2010), “A reinforced concrete frame element with shear effect”, *Struct. Eng. Mech.*, **36**(1), 57-78.
- Vecchio, F.J. and Collins, M.P. (1986), “The modified compression field theory for reinforced concrete elements subjected to shear”, *ACI Struct. J.*, **83**(2), 219-231.
- Vecchio, F.J. and Shim, W. (2004), “Experimental and analytical reexamination of classic concrete beam tests”, *J. Struct. Eng.-ASCE*, **130**(3), 460-469.
- Vulcano, A. and Bertero, V.V. (1987), *Analytical Models for Predicting The Lateral Response of R.C. Shear Walls: Evaluation of Their Reliability*, UCB/EERC-87/19.